(12)

DEVELOPMENT OF PHYSICAL TECHNIQUES FOR THE NON-
DESTRUCTIVE EVALUATION OF POLYMERS

Final Report

K H G Ashbee, P A Gass, J P Sargent

12

DEVELOPMENT OF PHYSICAL TECHNIQUES FOR THE   NON-
DESTRUCTIVE EVALUATION OF POLYMERS

Final Report

K H G Ashbee, P A Gass, J P Sargent

Reporting Period:
September 1985 September 1986

United States Army

EUROPEAN RESEARCH OFFICE OF THE U.S. ARMY

London   England

CONTRACT NUMBER DAJA45-85-C-0053

University of Bristol, H H Wills Physics Laboratory,
Bristol BS8 1TL

AI73 852

REPORT DOCUMENTATION PAGE

1a REPORT SECURITY CLASSIFICATION Unclassified	1b RESTRICTIVE MARKINGS
2a SECURITY CLASSIFICATION AUTHORITY	3. DISTRIBUTION/AVAILABILITY OF REPORT Approved for public release; distribution unlimited
2b. DECLASSIFICATION/DOWNGRADING SCHEDULE	

4. PERFORMING ORGANIZATION REPORT NUMBER(S)	5. MONITORING ORGANIZATION REPORT NUMBER(S) R&D 4804-MS-01

6a. NAME OF PERFORMING ORGANIZATION University of Bristol	6b. OFFICE SYMBOL (If applicable)	7a. NAME OF MONITORING ORGANIZATION USARDSG(UK)

6c. ADDRESS (City, State, and ZIP Code) H. H. Wills Laboratory Bristol BS8 1TL	7b. ADDRESS (City, State, and ZIP Code) Box 65 FPO NY 09510-1500

8a. NAME OF FUNDING/SPONSORING ORGANIZATION USARDSG-UK ARO-E	8b. OFFICE SYMBOL (If applicable)	9. PROCUREMENT INSTRUMENT IDENTIFICATION NUMBER DAJA45-85-C-0053

8c. ADDRESS (City, State, and ZIP Code) Box 65 FPO NY 09510-1500	10. SOURCE OF FUNDING NUMBERS			
	PROGRAM ELEMENT NO. 61102A	PROJECT NO 1L161102BH57	TASK NO. 04	WORK UNIT ACCESSION NO

11. TITLE (Include Security Classification)

(U) Development of Physical Techniques for the Non-Destructive Evaluation of Polymers

12. PERSONAL AUTHOR(S)
K. H. G. Ashbee, P. A. Gass and J. P. Sargent

13a. TYPE OF REPORT Final	13b TIME COVERED FROM 9/85 TO 9/86	14 DATE OF REPORT (Year, Month, Day) 1986, 9, 30	15 PAGE COUNT 39

16. SUPPLEMENTARY NOTATION

17.	COSATI CODES		18. SUBJECT TERMS (Continue on reverse if necessary and identify by block number)
FIELD	GROUP	SUB-GROUP	Polymeric materials, Composite materials, Epoxy, NDE, Interfacial debonding, Microstructural defects, Ultrasound visualisation, Microwaves,
20	06		
11	04		

19. ABSTRACT (Continue on reverse if necessary and identify by block number)

λ (Lambda)

Interfacial gaps between fibre and matrix materials in glass fibre reinforced composites influence both the distribution and phase properties of the reflected light. An ultrasound schlieren system has been used to model the optical reflection properties and visualise the wavefront trajectories for small interfacial gaps ($\lambda/30$). Quantitative estimates of the reflected light intensity for TE and TM modes, and the nature of the reflected phase properties, has been obtained from the "characteristic matrices" of tunnel and dielectric films. It is demonstrated that complete information about interface geometry, and hence debond geometry, can be derived from the study of the distributions of transmitted and reflected light. λ

20 DISTRIBUTION/AVAILABILITY OF ABSTRACT ☒ UNCLASSIFIED/UNLIMITED ☒ SAME AS RPT ☐ DTIC USERS	21 ABSTRACT SECURITY CLASSIFICATION Unclassified
22a NAME OF RESPONSIBLE INDIVIDUAL Dr. Iqbal Ahmad	22b TELEPHONE (Include Area Code) 01-409 4423	22c OFFICE SYMBOL AMXSN-UK-RM

18. Optics, Singularities, Catastrophe theory, Wavefront dislocations, Wavefront disclinations, S surfaces, C lines, Optical caustics, Optical tunnelling, Evanescent waves, Frustrated total internal reflection (FTIR), Schlieren images, Interferometry, Birefringence, Polarisation, Bi-dimensional compression, Fracture

19. Experiments have been conducted to exploit for polymer NDE purposes the singularity concepts of catastrophe theory. Disclinations, S surfaces and C lines are the singularites encountered in electromagnetism and preliminary experiments have been carried out using 60 GHz microwaves. These new methods for polymer NDE are especially aimed at the detection and sizing of small second phase particles, including microcracks. To this end, a bi-dimensional compression device has been used to effect controlled internal deformations of chalk filled PVC and rubber filled epoxy resin samples.

Accession For	
NTIS GRA&I	☒
DTIC TAB	☐
Unannounced	☐
Justification	

By	
Distribution/	
Availability Codes	

Dist	Avail and/or Special
A-1	

Abstract

Interfacial gaps between fibre and matrix materials in glass fibre reinforced composites influence both the distribution and phase properties of the reflected light. An ultrasound schlieren system has been used to model the optical reflection properties and visualise the wavefront trajectories for small interfacial gaps ($\lambda/30$). Quantitative estimates of the reflected light intensity for TE and TM modes, and the nature of the reflected phase properties, has been obtained from the "characteristic matrices" of tunnel and dielectric films. It is demonstrated that complete information about interface geometry, and hence debond geometry, can be derived from the study of the distributions of transmitted and reflected light.

Experiments have been conducted to exploit for polymer NDE purposes the singularity concepts of catastrophe theory. Disclinations, S surfaces and C lines are the singularites encountered in electromagnetism and preliminary experiments have been carried out using 60 GHz microwaves. These new methods for polymer NDE are especially aimed at the detection and sizing of small second phase particles, including microcracks. To this end, a bi-dimensional compression device has been used to effect controlled internal deformations of chalk filled PVC and rubber filled epoxy resin samples.

Introduction

Originally proposed as a two year program of research, the work described here was truncated on account of the principal investigator's departure to the USA after one year.

The study of schlieren images of ultrasound analogues to investigate the early stages of debonding in fibre reinforced plastics has been completed. So to have the preliminary experiments designed to exploit for polymer NDE purposes disclination structures in microwave fields; further experimentation will require substantial investment in microwave equipment.

With a view to using changes in microwave disclination structures to detect the onset of microcracking around micron and sub-micron size particles in polymers, a bi-dimensional compression device has been used to effect controlled internal deformations of chalk filled PVC and rubber filled epoxy resin samples.

(1) OPTICAL REFLECTION PROPERTIES OF DAMAGED COMPOSITES AND ULTRASOUND ANALOGUES

Casual observation of the optical reflection properties of a glass fibre reinforced composite which has sustained fibre/matrix interfacial damage, frequently reveals a characteristic pattern of diffuse light scattering, commonly known as fibre whitening, or fibre prominence. When viewed in transmission, this damage manifests itself as a reduction in the amount of light transmitted, giving the composite a darker appearance than it would if undamaged. In earlier papers by Sargent and Ashbee[1], and Sargent and Upstill[2], it was shown that this reduction in transmittance can be satisfactorily accounted for in terms of fibre debonding, the formation of interfacial gaps, and the phenomenon of frustrated total internal reflection (FTIR) whereby light, which is incident at angles greater than the critical angle ($>\theta_c$), optically tunnels across the interfacial gap. It was further shown that, by measuring the phase and transmittance properties of that proportion of light which optically tunnelled across the gap, measurement of nanometre gap widths could be made. Sargent and Ashbee[1] also considered the consequences of either water or air being present in the interfacial gap on its transmittance properties.

Figure 1 is a photomicrograph of a debonded fibre taken in reflected light; the non-uniform distribution of light is typical of fibres that have debonded. It is the purpose of this investigation to examine the microscopic reflection optical properties, with the aim of understanding how this pattern of light can be explained and, in particular, to show how such properties can be related to the diffuse light scattering phenomena described above.

REFLECTION PROPERTIES OF INTERFACIAL GAPS

In this analysis we assume the geometry shown in Figure 2. The boundary surfaces of fibre and matrix are assumed to be optically smooth surfaces. We consider as matrix a medium with refractive index n_3 in which is embedded a fibre of refractive index n_1, with an annular gap of refractive index n_2 between matrix and fibre. This is illuminated by a parallel (or nearly

parallel) beam of monochromatic light of free space wavelength λ, incident normal to the fibre axis. Typically $n_1 = n_3 \sim 1.55$ for matrix and fibre materials, and $n_2 = 1.0$ for air or vacuum.

Ray optics of interfacial gaps

When the interfacial gap is more than a few wavelengths wide, light is reflected and refracted in accord with geometrical optics. As an example, Figure 3 shows a geometrical optics ray diagram for light reflected from a fibre, surrounded by an interfacial gap of width measuring approximately 1/4 a fibre diameter. The proportion of light which is reflected is given by the Fresnel equations (Hecht and Zajac[3]), these equations relate the reflectance to the polarisation state, the angle of incidence, and the relative refractive indices of the media either side of an interface. At normal incidence Fresnel's equations predict that the reflectance at each interface will amount to approximately 4% of the incident energy, irrespective of polarisation state. At the polarising angle of about 56°, and for external reflection ($n_{transmitted} > n_{incident}$), the reflectance for TM mode (electric vector parallel to the plane of incidence) falls to 0%, and for TE mode (electric vector perpendicular to the plane of incidence) it is approximately 15%. At angles of incidence greater than the critical angle , and for internal reflection ($n_{transmitted} < n_{incident}$), then 100% of the light is reflected. Note that surfaces which are convex with respect to the incident light (such as the front surface of the fibre) give rise to diverging light, and surfaces which are concave with respect to the incident light (such as the rear surface of the fibre) give rise to focussing and result in the formation of caustic surfaces. When they appear in the field of view, such caustics dominate the microscope image. Note also that the interfacial gap behaves as an optical cavity within which optical interference can take place, as a result of which the overall reflected intensity will be a function of interfacial gap width. In addition, diffraction effects from boundarys like that provided by the interfacial gap will be apparent.

Ultrasound visualisation

In reality, interfacial gaps will usually be much smaller than that shown in Figure 3, and for gaps $<\sim \lambda$, a significant proportion of the light which, with larger interfacial gaps, would normally be totally internally reflected will instead optically tunnel across the interfacial gap. As an aid to an understanding of how this might be expected to affect the distribution of reflected light, the ultrasound schlieren system shown in Figure 4 was constructed. The system provides an ultrasound analogue of the above optical problem. By pulsing a light source in synchronism with the generation of ultrasound wavefronts, with a variable delay between light pulse and wavefront, visualisation of the wavefront as it propagates through the specimen can be achieved. A short cylindrical pipe was fabricated from aluminium foil with dimensions, measured in ultrasound wavelengths, the same as the dimensions of the fibre/matrix/interfacial gap measured in optical wavelengths. The wall thickness of the front half-cylinder of the aluminium pipe was made to be 0.06λ, and that of the rear half-cylinder 0.3λ. With this geometry, angles of incidence greater than the critical angle produced internal reflection frustrated in a sense similar to that for light incident on a debonded fibre. The velocity of sound in the visualising medium (water)

2

is less than that in aluminium, so the relative refractive indices bear a similar relationship to those of matrix or glass and air.

Figure 5 shows a sequence of schlieren images photographed as the wavefront for a single pulse propagated through the visualising medium (the 5 MHz compression wave ultrasound transducer is located above the aluminium tube, which is itself seen end-on in the Figure). The incident compressional wave is mode converted by the front surface of the tube, and compressional and shear waves propagate across the wall (the critical angle for compressional waves propagating through the aluminium is 14°, and that for shear waves is 29°). The wavefront propagates across the the entire front surface essentially undeviated (horizontal band of white contrast in Figure 5a), with a proportion of the incident energy reflected back towards the transducer as a diverging wavefront (semi-circular band of white contrast in Figure 5a). The transmitted wavefront continues to propagate across the bore of the pipe until it suffers reflection at the rear internal surface and is brought to a focus just above the rear internal surface (Figure 5b). This wavefront continues to propagate upwards diverging from its focus (Figure 5c), further reflections taking place on the inner side walls of the pipe giving rise to side-lobes (one of which is indicated by an arrow in Figure 5d). A proportion of the wavefront then propagates back through the front wall of the pipe whilst a proportion is reflected from the inner front surface, and is brought to a second focus (Figure 5e). The "trapped" wavefront propagates backwards and forwards inside the pipe, with intensity gradually reducing. Notice that the focussed structures are not uniformly bright, but instead reveal interference detail attributable to the wave nature of the ultrasound.

The focussing action of the rear inner surface is illustrated by the ray diagram in Figure 6. Rays are shown incident on half of a semi-circle and give rise to a central and to two side caustic curves, after 1, 2 and 3 reflections by the rear inner surface respectively. These correspond, 1 to the bright central focussed region seen in Figure 5b, and 2 and 3 to the side lobes in Figure 5d respectively. The same effect with a debonded fibre can be illustrated by arranging for only half of the fibre to be illuminated, (Figure 7). Note that the fibre is bright only on the side remote from the illumination, and not adjacent to it. This we interpret as indicating that the light has suffered 2, 3 or more reflections at the rear region of interfacial debonding in the manner described above.

Except for drawing attention to some interference structure revealed in Figure 5, we have so far ignored the consequences of interference. The schlieren system, used in a continuous wave mode to visualise standing wave patterns (Figure 8) reveals a complicated set of interference phenomena. If it were possible to resolve fine detail in the optical images, a similar complex pattern of interference is expected.

Physical optics of interfacial gaps

Ultrasound images of the kind discussed above provide a guide to the wavefront trajectories and interference structures encountered when light traverses a debonded fibre. However in order to take into account the polarisation properties and hence estimate quantitatively the proportion of light reflected at each interface for such small gaps, it is necessary to make recourse to the techniques of physical optics and the concepts of evanescent waves.

3

The interfacial gap can be approximated as a series of parallel-sided films (refractive index 1.0) located between two homogeneous media of refractive index n_1. Born and Wolf[4] show how the reflectance and polarisation properties of such a thin dielectric film may be obtained by use of a characteristic matrix describing its optical properties. We show here how the equivalent characteristic matrix for a tunnel film can be used to derive the reflection coefficients and polarisation properties for a film in which optical tunnelling occurs.

From equations given by Born and Wolf[4], it is possible to derive the characteristic matrix (M) for a tunnel film situated between two dielectric layers

$$M = \begin{bmatrix} \cosh\beta' & \dfrac{-i\sinh\beta'}{p_2'} \\ -ip_2'\sinh\beta' & \cosh\beta' \end{bmatrix} \tag{1}$$

where $p_2' = (n_1 \sin^2\theta_i - 1)^{1/2}$

θ_i = incident angle

$\beta' = 2\pi d p_2'/\lambda_o$

d = interfacial gap width

λ_o = free space wavelength

the reflection coefficient r, is given by Born and Wolf[4] as

$$r = \frac{(m_{11}' + m_{12}'p_1)p_1 - (m_{21}' + m_{22}'p_1)}{(m_{11}' + m_{12}'p_1)p_1 + (m_{21}' + m_{22}'p_1)}$$

where m_{ij}' are the matrix elements of the characteristic matrix, and $p_1 = n_1\cos\theta_i$ for TE mode and $p_1 = \cos\theta_i/n_1$ for TM mode, thus substitution for m_{ij}' gives

$$r = \frac{-i\sinh\beta' \ (p_1^2 + p_2'^2)}{2p_1 p_2'\cosh\beta' + i\sinh\beta' \ (-p_1^2 + p_2'^2)} \tag{2}$$

For completeness we also show the characteristic matrix for a dielectric film (i.e. for incident angles $<\theta_c$)

$$M = \begin{bmatrix} \cos\beta & \dfrac{-i\sin\beta}{p_2} \\ -ip_2\sin\beta & \cos\beta \end{bmatrix} \tag{3}$$

where $p_2 = (1 - n_1 \sin^2\theta_i)^{1/2}$

$\beta = 2\pi d p_2/\lambda_o$

and substituting for m_{ij}' gives

$$r = \frac{i\sin\beta \ (p_1^2 - p_2^2)}{2p_1 p_2\cos\beta - i\sin\beta \ (p_1^2 + p_2^2)} \tag{4}$$

4

the reflectance (R) is related to the reflection coefficient (r)

$$R = |r|^2$$

We can also derive the phase shift (ϕ_r) on reflection, thus for $\theta_i > \theta_c$

$$\tan(\phi_r) = \frac{\text{Im}(r)}{\text{Re}(r)} = \frac{2p_1 p_2' \cosh\beta'}{(p_2'^2 - p_1^2)\sinh\beta'} \tag{5}$$

and for $\theta_i < \theta_c$

$$\tan(\phi_r) = \frac{\text{Im}(r)}{\text{Re}(r)} = \frac{-2p_1 p_2 \cos\beta}{(p_2^2 + p_1^2)\sin\beta} \tag{6}$$

where the symbols have the same meanings as for equations (1) and (3) above.

The reader should be aware that in the above analysis no attempt has been made to describe diffraction effects, and in order to do so would require the use of exact scattering theory, this is however beyond the scope of the present treatment and the interested reader is referred to Sargent and Upstill[5] for a brief discussion of the applicability of this technique to specimens having the geometry described above.

In Figures 9(a) and (b) the reflectance for both TE and TM mode polarisation are shown as a function of angle of incidence from $0°$ to $90°$, and as a function of interfacial gap width from 0 to 1λ calculated as described above. Note that, for either polarisation mode, the proportion of light reflected increases monotonically with gap width up to $\lambda/4$, irrespective of incident angle. In Figure 10 is shown the phase difference surface $\phi_r(\text{TE}) - \phi_r(\text{TM})$, also calculated as described above.

Figure 11 is a photomicrograph of a debonded fibre viewed in reflected light under parallel polars and oriented for (a) TE mode and (b) TM mode. Note that, two side lobes are visible in Figure 11(a), but only one is visible in Figure 11(b), this can be explained by reference to Figure 9 and Figure 6; In Figure 6, the caustic surfaces formed by two reflections (inner of the two side caustics) from the rear surface are generated by rays which are incident on the rear interface at angles in the region $40° - 45°$, and it is at appr...mately $40°$ that the reflectance for TM mode (Figure 9(b)) falls to zero for all gap widths, thus the inner side lobe is suppressed. In Figure 11(c) the fibre axis is oriented at $45°$ to the polarising axes of crossed polars; a phase shift difference $\phi_r(\text{TE}) - \phi_r(\text{TM})$ takes place at each reflection on the rear region of interfacial debonding in the manner shown in Figure 6. In doing so, the plane of polarisation is rotated and this rotation gives rise to the bright banded appearance of the fibre. It should also be noted that there may be an additional phase shift difference introduced during transmission through the front region of debonding (for an explanation of this effect see Sargent and Upstill[2]. It is also evident that the central region of reflected light is much dimmer than the multiply reflected side lobes; this can be explained using Figure 10, very little phase shift difference is introduced at angles near normal incidence relative to that introduced at larger angles of incidence.

When observations of debonded fibres are made with transmitted light alone, it is not possible to decide whether an interfacial gap has equal width around its circumference. Thus, in Figure 12(a), which is a parallel polars transmission photomicrograph, the dark bands running parallel to the fibre axis indicate that debonding has occured but do not indicate whether the front face or rear face has debonded. Similarly in Figure 12(b), this is a crossed polars transmission photomicrograph of the same fibre but oriented at 45° to the polarisation axes, the debonded regions which show dark in Figure 12(a) now show up bright against a dark background, this occurs because of the rotation of the plane of polarisation upon transmission through the interfacial gaps. If the same fibre is now examined in reflection between crossed polars, from above and then from below the fibre axis, and providing that the width of the front interfacial gap is not so large as to prevent light from entering and leaving the fibre (this can be determined from a crossed polars transmission image of the fibre like that shown in Figure 12(b)), it is possible to resolve this ambiguity; regions that appear bright indicate that reflection has taken place from a debonded region on the rear surface. In Figure 12(c) is shown such an image photographed from above the fibre axis and in Figure 12(d) (which has been photographically reversed) the image from below. Figure 12(e) shows the debond geometry in schematic form.

(2) SINGULARITIES IN MICROWAVE FIELDS

Wavefront singularities in optical, ultrasound and microwave wavefields are potentially useful for the detection of microstructural defects within polymeric materials. They can be observed when a material containing defects is illuminated with a plane monochromatic wave and they provide an economical method of characterising the significant features of the wavefield. They are the result of interference effects when a defect acts as a scattering centre from which new wavefronts originate.

When a scalar monochromatic wave is scattered by a fixed object it produces a stationary three dimensional interference pattern where the singularities can be characterised by the patterns of dislocation lines, regions where the amplitude is exactly zero and the phase is indeterminate. When a vector monochromatic wave is used as a source of illumination then additional features are required to fully characterise its properties — these are known as disclinations, S surfaces and C lines, and are properties of the phase and polarisation structure of the electric and magnetic vector fields.

Direct observations of wavefront dislocations in scalar fields have been made for ultrasound, for example in two experiments by D R Andrews and in an independent experiment by G J Hardy. All three experiments make use of a light-emitting diode as a stroboscopic light source (Andrews and Wallis[6]), in a schlieren system by Andrews[7] and in a photoelastic system by Hardy et al[8].

Direct observations of wavefront singularities in vector electromagnetic wavefields have been made in microwave and in optical wavefields, by Hajnal[9]. These experiments were performed to verify the many aspects of the current theory of singularities as proposed by Nye[10,11,12]. Wavefront singularities have also been observed (though not reported as such) in microwave antennae literature[13], and in the electromagnetic theory of diffraction[14].

6

Definitions

The singularities that can exist in monochromatic wavefields, viz. disclinations, S surfaces and C lines, have been identified by Nye[10,11,12]. In the scalar wave approximation, i.e. that excluding polarisation effects, catastrophe optics and dislocation theory are sufficient to describe the features of the wavefield. However, in order to extend this theory to electromagnetism it is a further requirement that account be taken of the vector nature of electromagnetic waves. This then characterises the various aspects of the electric and magnetic fields. In a paraxial field it is possible to define the 3 classes of singularities:

1) C lines are singularities in the orientation of the polarisation ellipse of the transverse fields i.e. regions where $\underline{E}_T$ or $\underline{H}_T$ is circularly polarised.

2) S Surfaces are regions where the hand of polarisation is indeterminate, i.e. regions where $\underline{E}_T$ or $\underline{H}_T$ is linearly polarised.

3) disclination lines are lines where the instantaneous directions of $\underline{E}_T$ or $\underline{H}_T$ is undefined, i.e. regions where $\underline{E}_T$ or $\underline{H}_T = 0$.

In monochromatic E-M waves C lines and S surfaces are stationary, whereas disclination lines are often helical or in the form of closed loops. Disclination lines have the additional feature that they only begin or end on a boundary.

Hajnal[9] has experimentally observed all 3 classes of singularities in 8.5 GHz microwave fields, and has produced maps of the topological structure of the resulting fields. Typical configurations of the field patterns showing the singularity features are shown in Figure 13. Singularities in the radiation pattern of a parabolic reflector are shown in Figure 14, and in the diffraction pattern of electromagnetic waves in Figure 15.

In the present work it was anticipated that the construction of similar maps at 60 GHz would also reveal singularity features of the kind shown in Figure 13 after the waves had traversed a polymer containing defects. It was further anticipated that the location and identity of defects might be deduced from these maps.

Preliminary microwave experiments

The choice of the operating frequency used here (60 GHz) was made on the basis of the small size (~ 1µm) of defects to be detected, physical size of the apparatus, and the necessity of sufficient dielectric constant difference between defect and polymer to give rise to scattering. We were working to a reduced budget and were obliged to rely on casual use of 60 GHz equipment which belonged to the University's Department of Electrical and Electronic Engineering.

In order to locate the positions of the singularities in the wavefield it is first necessary to gather the phase and polarisation properties of the field, from which the singularity structure can be deduced. This may be done by either of two methods, both of which involve mechanical scanning of a receiving probe over a region of space. To this end, an XYZ computer

7

controlled scanning and data aquisition system was constructed, and interfaced with an existing microcomputer system which provided the necessary analysis and graphics display options. Figure 16 shows a general view of the apparatus.

To demonstrate that 60 GHz microwaves are scattered by defects of interest a transmittance image of a specimen was obtained using the apparatus. Figure 17 shows a GRP laminate which has suffered delamination during reverse bend fatigue; (a) is the laser beam optical transmittance and (b)-(f) are various 60GHz microwave transmittance images. It is evident that regions of delamination which scatter light also scatter the microwave radiation.

That the optical transmittance method used to obtain Figure 17(a) faithfully records the accumulation of mechanical damage has been established by carrying out real time digital image subtraction on a specimen whilst undergoing reverse bend fatigue. An example of images illustrating progressive accumulation of damage is shown in Figure 18.

In order to recover the phase and polarisation in addition to the intensity it is necessary to employ polarisation and phase sensitive detectors. Initially it was intended to adopt the technique used by Hajnal[9] and shown schematically in Figure 19. However, at 60 GHz this method was way beyond our budget and instead recourse was made to a far less expensive method employing reference beams and interferometry. The technique used was based on the Twyman-Green interferometer, Figure 20.

If the specimen is removed from Figure 20, then the superposed plane waves from M1 and M2 are exactly parallel and there is a constant phase difference between the superposed disturbances. The field is then of uniform intensity. If now the specimen is introduced in one of the arms as shown, phase disturbances from defects will be imposed on the plane wave. The wave from M2 will no longer be plane and interference fringes will be observed. These fringes, if they are perfect, are the disclinations of singularity theory. Adding an additional plane wave to this field using the plane mirror M1 would then permit a detailed investigation of the phase structure in the region of the disclination. By varying the plane of polarisation of the incident radiation it should also be possible to determine polarisation information from which full details of the singularities described above could be extracted. However, this demands careful interpretation since the plane of polarisation is altered upon reflection at non-normal angles of incidence, due account of which would have to be taken since the experimental setup includes several surfaces.

As a preliminary test to demonstrate that phase retreival is possible in an interferometer employing microwaves, a simple Fizeau arrangement was constructed, in which partially aluminised expanded polystyrene flats formed the surfaces of the cavity within which interference took place. Figure 21 shows the interference pattern recorded when the flats were oriented with a small angle between their reflecting surfaces. The dark bands are the interference fringes and record phase contours with spacing 2π.

In order to form an image in the plane of the specimen and also to produce a collimated beam of microwaves, it was necessary to employ accurately fabricated parabolic mirror surfaces large enough that any fabrication defects would not contribute significant errors to the phase measurements. We were obliged to attempt our own fabrication of mirrors and this we did

using GRP moulding techniques. To date satisfactory mirrors have not been produced.

(3) BI-DIMENSIONAL COMPRESSION

Figure 22 illustrates a method whereby bi-dimensional compression can be applied to bar stock of rectangular cross-section. The four working components are identical gee-shaped elements. A working model of this apparatus has been described by Ashbee[15].

Here, a 10,000 psi hydraulically driven bidimensional compression apparatus was used for the experiments.

Bi-dimensional compression of chalk filled PVC

Let x and y be the directions of displacement produced by advancing the two pairs of orthogonally opposed gees and let z be the direction normal to plane xy. Identical displacement along x and y creates 2-dimensional compression in plane xy and this is equivalent to uniaxial tensile strain along z. Independent displacement along x and y creates a state of triaxial strain, viz the two independent strains imposed in the x and y directions and the strain along z that is determined by the condition of (near) incompresssibility of the specimen. Displacement in only one direction, say x, creates the state of strain x < 0, y = 0, z > 0, i.e. a state of strain equivalent to pure shear.

$$\lambda_1 \ \lambda_2 \ \lambda_3 = 1$$

where λ_1, λ_2 and λ_3 are the extension ratios along the x, y and z directions

With no stress in the z-direction,

The stress along x,
$$t_{xx} = 2(\lambda_1^2 - \lambda_3^2)\left(\frac{\partial W}{\partial I_1} + \lambda_2^2 \frac{\partial W}{\partial I_2}\right)$$

and the stress along y,
$$t_{yy} = 2(\lambda_2^2 - \lambda_3^2)\left(\frac{\partial W}{\partial I_1} + \lambda_1^2 \frac{\partial W}{\partial I_2}\right)$$

where
$$I_1 = \lambda_1^2 + \lambda_2^2 + \lambda_3^2$$

$$I_2 = \frac{1}{\lambda_1^2} + \frac{1}{\lambda_2^2} + \frac{1}{\lambda_3^2}$$

For a Rivlin material, the energy function $W = C_1 (I_1 - 3)$

For a Mooney-Rivlin material, $W = C_1 (I_1 - 3) + C_2(I_2 - 3)$

i.e.
$$\frac{\partial W}{\partial I_1} = C_1, \quad \frac{\partial W}{\partial I_2} = C_2$$

Therefore

$$t_{xx} = 2(\lambda_1^2 - \lambda_3^2)(C_1 + \lambda_2^2 C_2)$$

$$t_{yy} = 2(\lambda_2^2 - \lambda_3^2)(C_1 + \lambda_1^2 C_2)$$

where C_1 and C_2 are constants

Tests were performed using the bidimensional rig on specimens of chalk filled PVC in an attempt to determine the constants C_1 and C_2. Figure 23 shows the data plotted as $\partial W/\partial I_2$ versus I_2 for constant I_1. It is evident that no useful conclusions can be drawn from these data. However, in Figure 24 we plot $(t_1 - t_2)$ versus $(\lambda_2^2 - \lambda_1^2)$ from which we deduce a value of 5 bars (5×10^5 Nm^{-2}) for the shear modulus.

Large plastic bi-dimensional deformation of the chalk filled PVC resulted in volume expansions of approximately 40%. Figure 25(a) shows the specimen in its initial undeformed state, and in (b) and (c) the results of two compression tests, illustrating the large permanent volume expansions obtained. The occurence of cavitation adjacent to the hard second phase materials is evident in Figure 26 which shows stereo pair photomicrographs of sections from planes taken (a) parallel and (b) perpendicular to the long axis of the deformed specimen. There is increased granularity in sections like that shown in (b) from which it is deduced that a marked texture of cracks exists running across the specimen width and perpendicular to the long axis.

Bidimensional compression of a rubber particle filled epoxy resin

The purpose of the experiments is to determine whether or not the compression-compression quadrant for an epoxy resin is open in the manner of Griffith.

The resin selected for this study, Hexcel F-185, was available both with and without 11% by volume of rubber particulate toughening agent. Samples of each were subjected to bi-dimensional compression. One batch of test-pieces of both materials was milled to have the dimensions 7/8"x7/8"x9/16". A second batch was milled to have the dimensions 3"x0.608"x0.608".

All of the tests reported were carried out at room temperature (23°C). The full 10,000 psi ram pressure was applied as quickly as possible, i.e. within 30 seconds. The pistons through which the pressure was transmitted to the gee-shaped elements were each of cross-sectional area 5 in^2. Hence the bidimensional compression force applied to the specimen was 15,000 lbs.

Specimen dimensions (")	Neat Resin		Rubber Toughened Resin	
	Initial Bidimensional Compressive Stress (psi)	Extensional Strain (%)	Initial Bidimensional Stress (psi)	Extensional Strain (%)
7/8x7/8x9/16	19,500	390	19,500	373
7/8x7/8x9/16	1,300	182	600	154
3x0.608x0.608	8,250	16	8,250	40
3x0.608x0.608	550	2	8,250	41

None of the specimens tested experienced failure and the very large extensional strains are to be compared with the uniaxial tensile strain to failure of 9.5% quoted in the manufacturer's data sheet.

PUBLICATIONS

"Detection and measurement of very small interfacial gaps in GRP"
J P Sargent and K H G Ashbee
Composites Science and Technology, (1985), 22, 135-152

"Aviation fuel uptake by epoxy adhesives"
J P Sargent and K H G Ashbee
J.Adhesion, (1985), 18, 217-227

"The detection of debonding in GRP using evanescent waves"
M P Clarke, P A Gass and J P Sargent
NDT International, (1985), 18, 345-351

"Mode III fracture toughness of glassy and crystalline silicates"
D A Tossell, J P Sargent and K H G Ashbee
In "Science of Hard Materials" Proceedings of the International Conference on the Science of Hard Materials, Rhodes, Greece 23-28 September 1984, Ed E A Almond, C A Brookes and R Warren, Inst. Phys. Conf. Ser. No 75: (1986), Chap 5, 459-471

"Polymer NDE"
K H G Ashbee, (ed.)
Published by Technomic (1986), 332 +xiv pp.

"The propagation of light through fibre reinforced composites"
J P Sargent and C Upstill
In "Polymer NDE" ed. K H G Ashbee, Published by Technomic (1986), 195-213

"Optical tunnelling through interfacial gaps in fibre-reinforced composites"
J P Sargent and C Upstill
Composites, (1986), 17, 49

"The reflection properties of debonded fibres in GRP"
J P Sargent and P A Gass
J. Phys. D., (1986), 19, 897

"Bi-dimensional compression moulding of super-high fibre volume fraction composites"
K H G Ashbee
J. Comp. Mater., (1986), 20, 114

"The role of water of crystallization in the swelling of corrosion products"
K H G Ashbee and L R Cornwell
Scripta Met., (1986), 20, 605-608

REFERENCES

1) Sargent, J.P. and Ashbee, K.H.G., (1985), Composites Science and Technology, $\underline{22}$, 135
2) Sargent, J.P. and Upstill, C., (1986), Composites, $\underline{17}$, 49
3) Hecht, E. and Zajac, A., "Optics", (1974), (Reading, Mass.: Addison Wesley), 72
4) Born, M. and Wolf, E., "Principles of Optics", (1965), (Oxford: Pergamon Press), 55
5) Sargent, J.P., and Upstill, C., (1986), in "Polymer NDE" ed. K.H.G. Ashbee (Westport, CT, USA: Technomic), 195
6) Andrews, D.R. and Wallis, L.J., (1977), J. Phys. E., $\underline{10}$, 95
7) Andrews, D.R., (1983), 15th Intl. Congr. on High Speed Photography and Photonics, Soc. of Photo-Optical Instrumentation Engrs., 348, 565
8) Hardy, G.J., Turner, T.W. and Ashbee, K.H.G., (1978), Metal Sci., $\underline{12}$, 406
9) Hajnal, J.V., (1985). "Singularities in monochromatic electromagnetic waves" Ph. D. thesis, University of Bristol
10) Nye, J.F., (1981), Dislocations and disclinations in transverse e-m waves. In: Balian, R. et al (eds) "Les Houches, Session XXXV, 1980 – Physics of Defects". Amsterdam: North Holland Publishing Company
11) Nye, J.F., (1983a), Proc. R. Soc. Lond. $\underline{A387}$, 105-132
12) Nye, J.F., (1983b), Proc. R. Soc. Lond. $\underline{A389}$, 279-290
13) Monich, G., (1981), IEE Conference "ICAP", held at York, England
14) Braunbek, W. and Laukien, G., (1952), Optik, $\underline{9}$, 174
15) Ashbee, K.H.G., (1986), J. Comp. Mater., $\underline{20}$, 114-124

Figure 1   Optical reflection photomicrograph of a debonded fibre. Fibre
diameter is approximately 10µm (45 optical wavelengths).
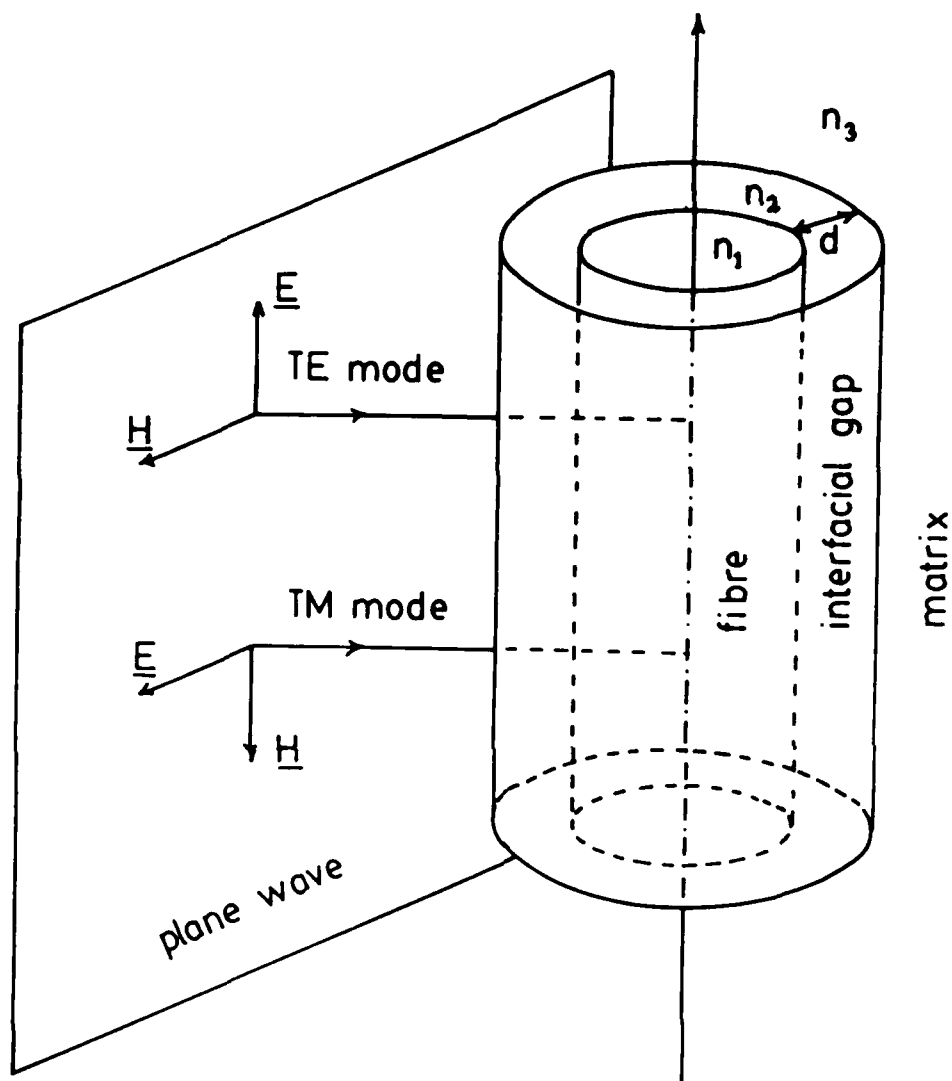
Figure 2   Optical geometry for a model composite specimen comprising a glass fibre (refractive index n_1) surrounded by a concentric annular interfacial gap (n_2) contained within a resin matrix (n_3).
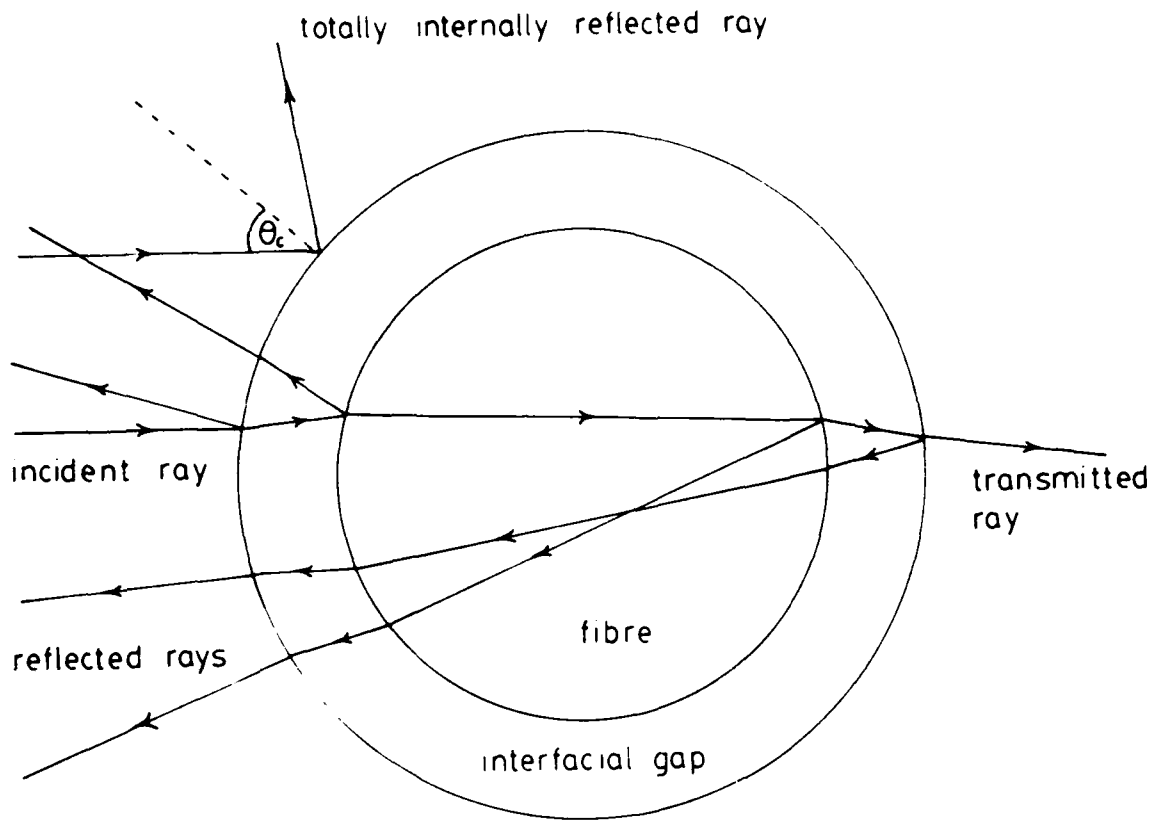
Figure 3   Ray diagram for plane parallel light incident upon a glass fibre
embedded in resin with an air gap at the interface. Interfacial
gap is 1/4 a fibre diameter.
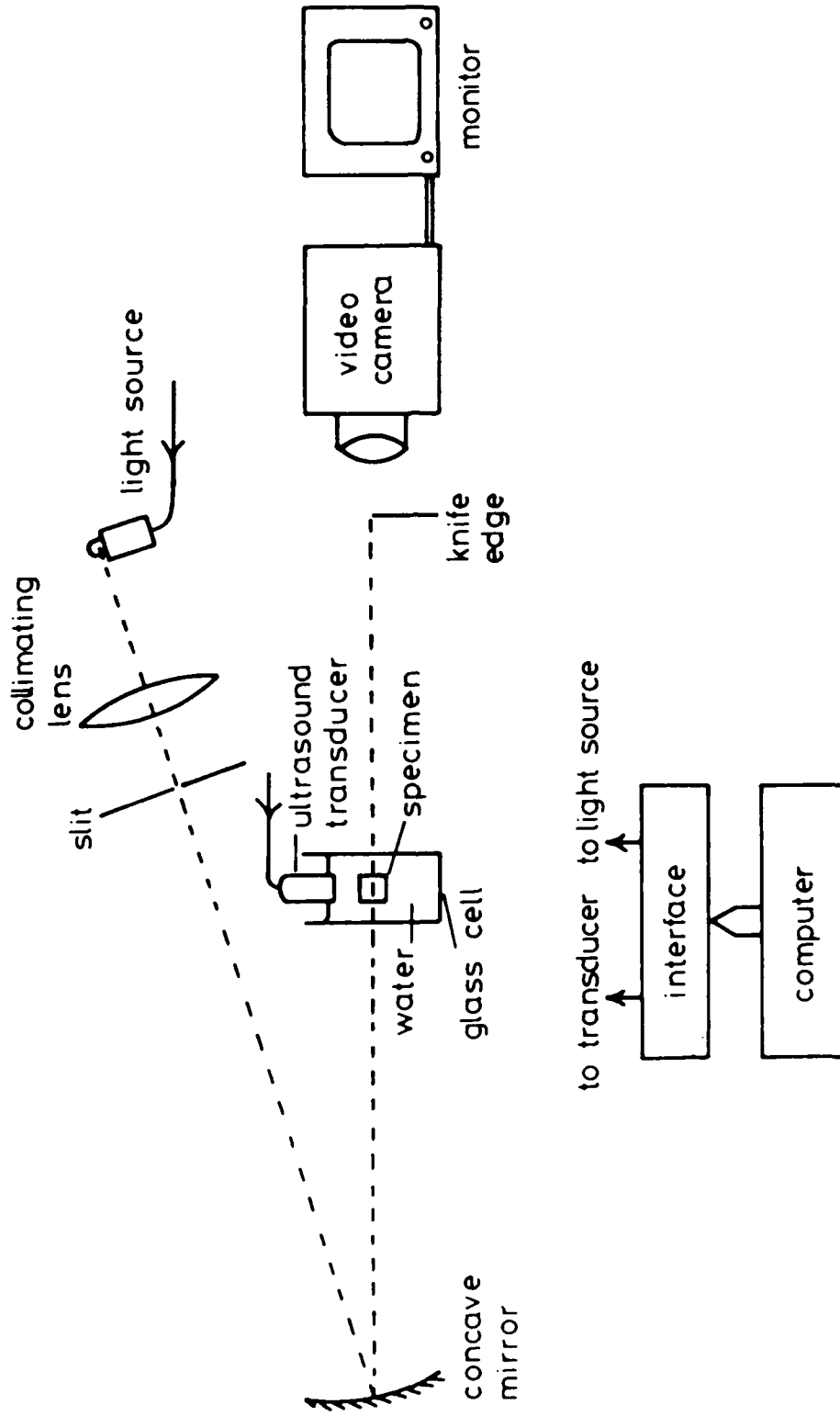
Figure 4   Schematic diagram showing the main components of the computer controlled ultrasound schlieren system.
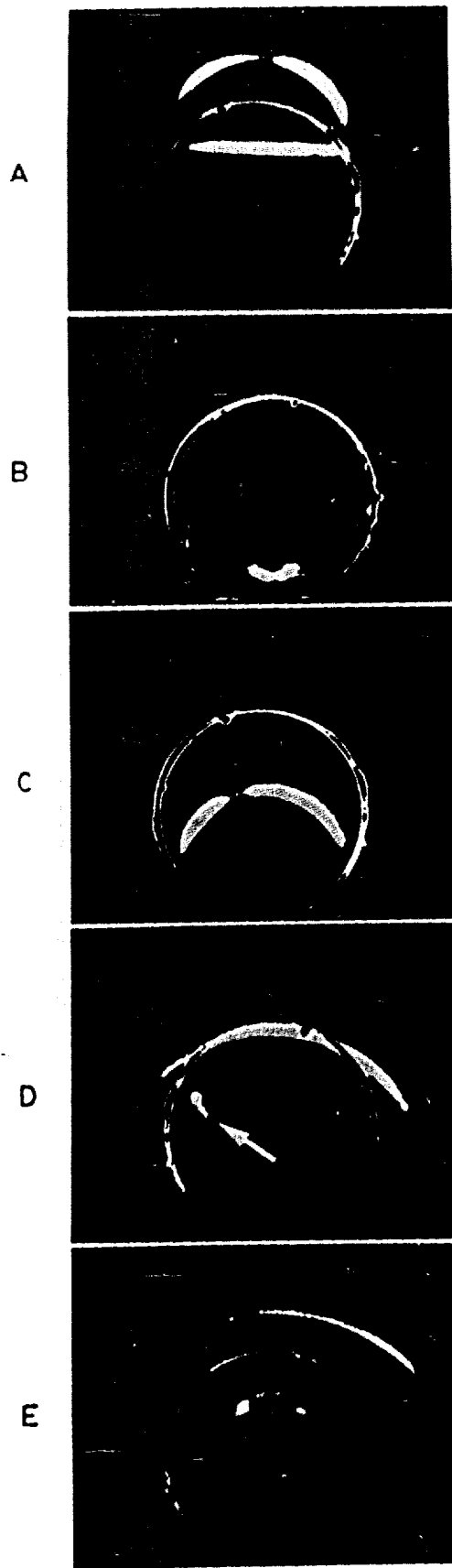
Figure 5   Schlieren images of a single ultrasound wavefront propagating
through a thin walled aluminium foil pipe. The top half of the
pipe has a wall thickness of 0.06 ultrasound wavelengths and the
bottom half has a wall thickness of 0.3 ultrasound wavelengths.
The pipe diameter is approximately 15mm (50 ultrasound
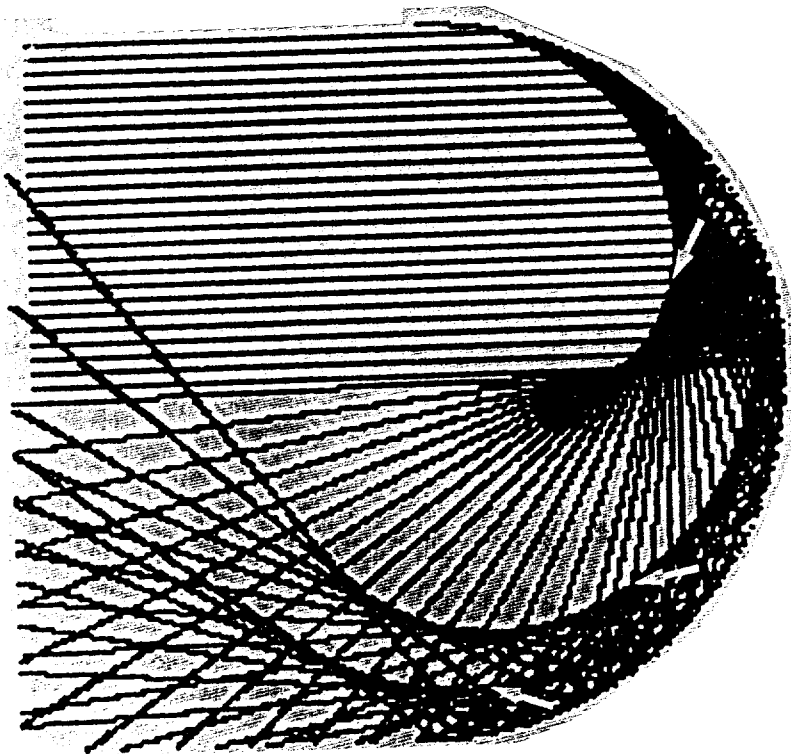
Figure 6   Ray diagram illustrating multiple reflections and the formation of caustic surfaces (indicated by arrows).
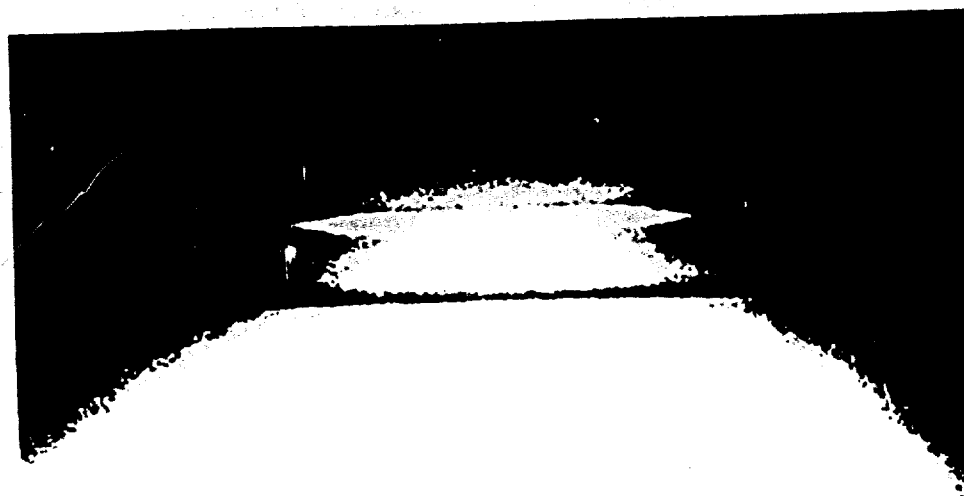
Figure 7   A debonded fibre photographed with reflected light. The light is
incident on only one half of the fibre diameter.
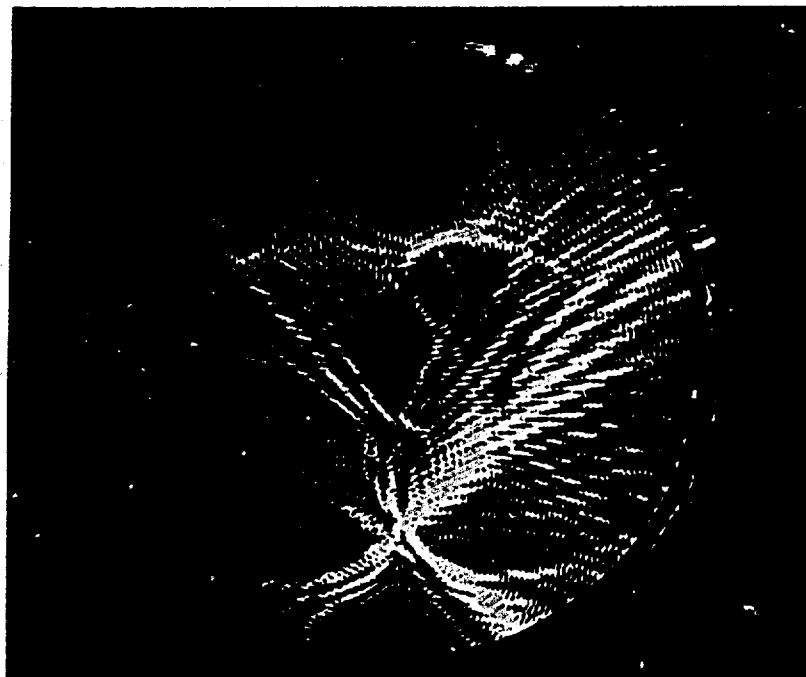
Figure 8   Standing wave ultrasound pattern for the aluminium foil pipe studied in Figure 3.
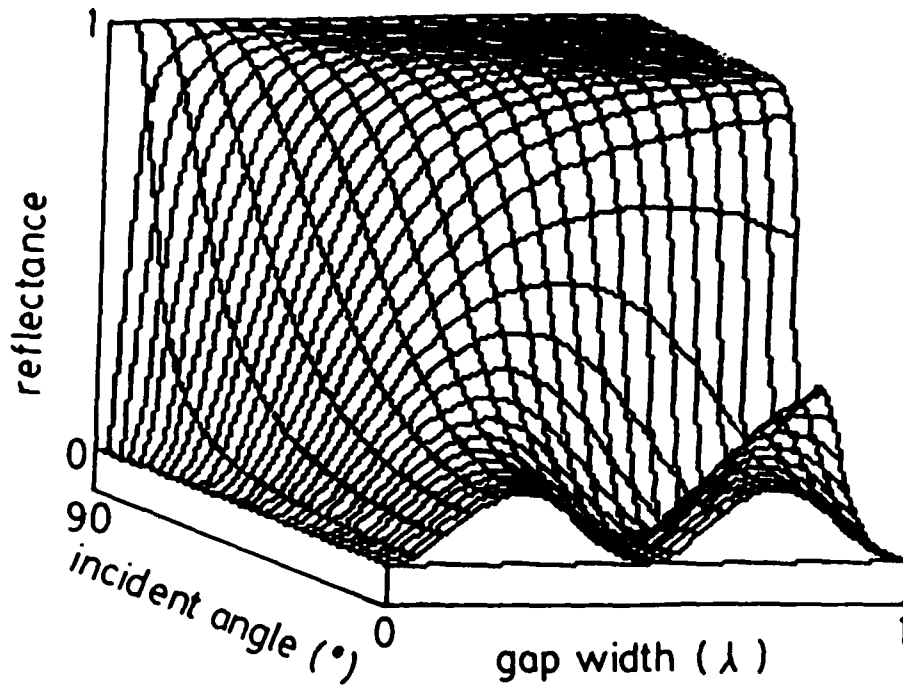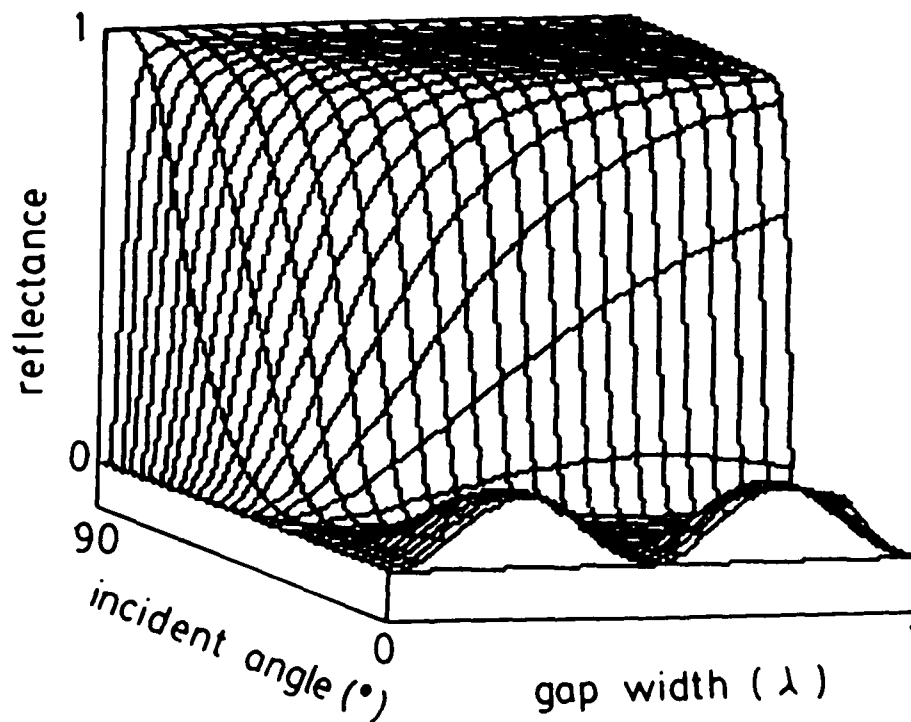
Figure 9(a) The reflectance (TE mode) as a function of gap width and incident
            angle. Gap width interval 0.05λ, incidence angle interval 2.86°.
      (b) Same as (a) but for TM mode.
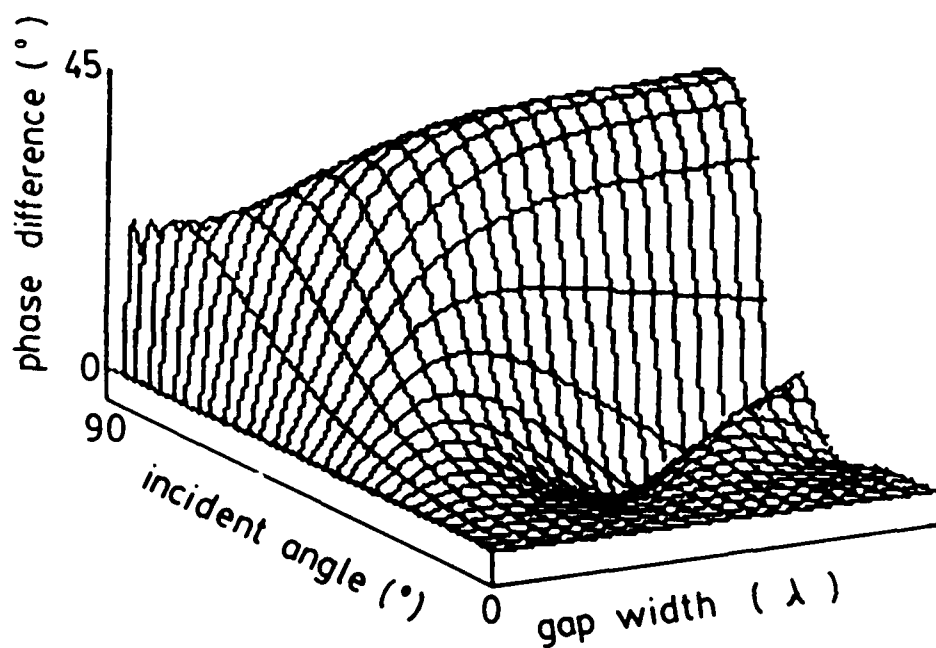
Figure 10   The phase difference between the TE mode and TM mode polarisation
             components $(\phi_r(TE) - \phi_r(TM))$ reflected from the interfacial gap.
             Gap width interval 0.05λ, incidence angle interval 2.86°.
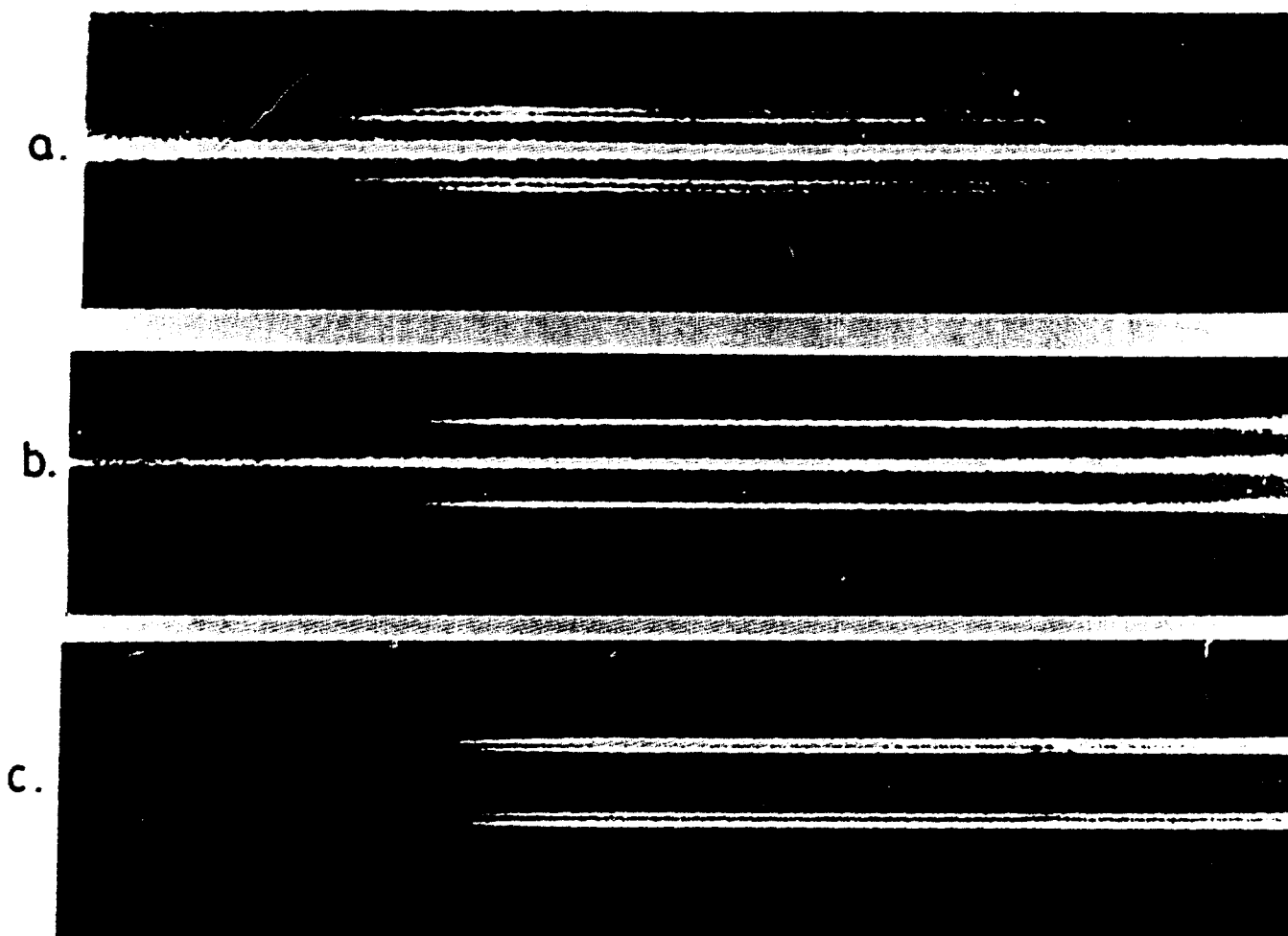
Figure 11   Photomicrographs of a debonded fibre in reflected light showing its appearance when viewed (a) with the optic axis of the polariser parallel to the fibre axis (TE mode), (b) with optic axis of the polariser perpendicular to the fibre axis (TM mode), and (c) between crossed polars and oriented at 45° to the axes of polarisation.
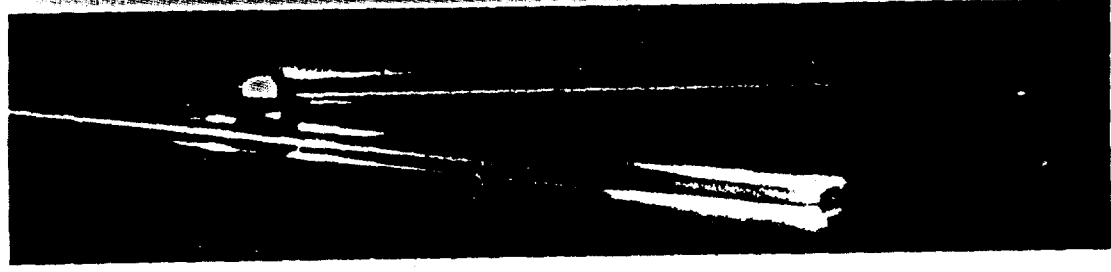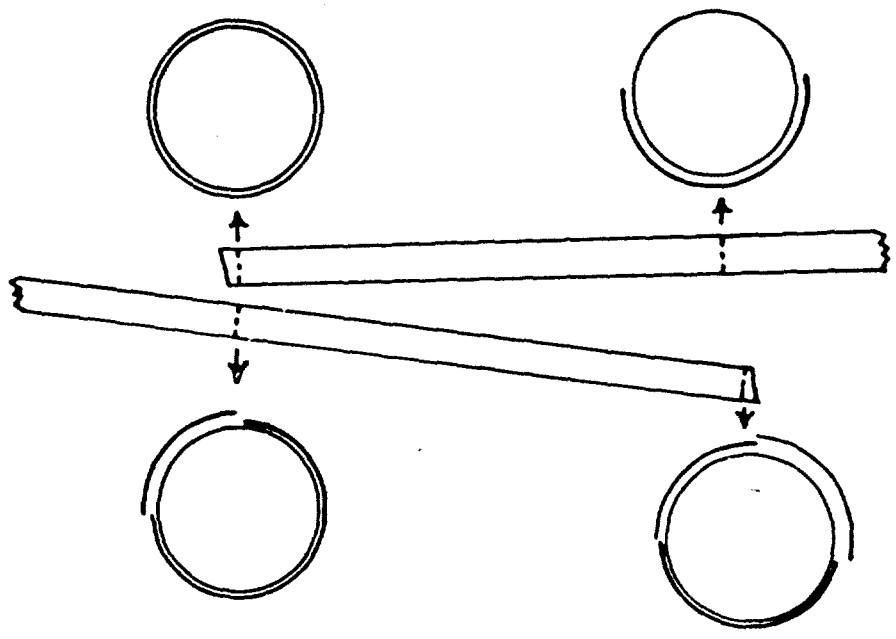
Figure 12(a) Parallel polars transmission photomicrograph of a debonded fibre
(b) Crossed polars transmission image of (a)
(c) Crossed polars image of (a) but viewed with reflected light and from above the fibre axis,
(d) Same as (c) but viewed from below the fibre axis and photographically reversed
(e) Schematic diagram showing the debond geometry
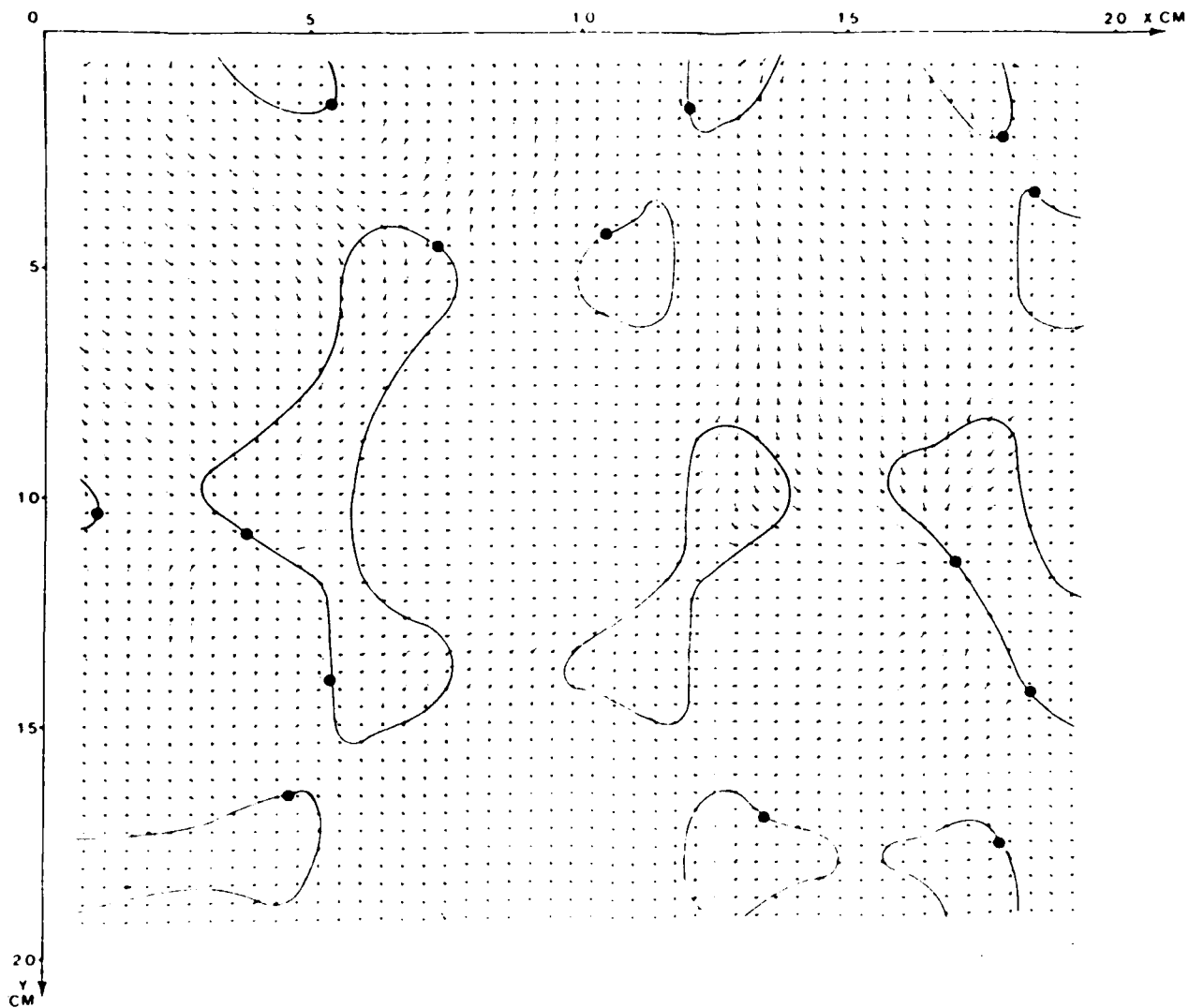
Figure 13   Map   of   directions of $\underline{E}_T$ in the z=8mm plane of the 4-beam   field
            when ωt=0. The   direction   of $\underline{E}_T$ at each   measurement   site   is
            indicated by a directed line element with a dot to represent   the
            head   of   the electric vector. Large dots mark d   points,   solid
            lines indicate s contours. After Hajnal[9].
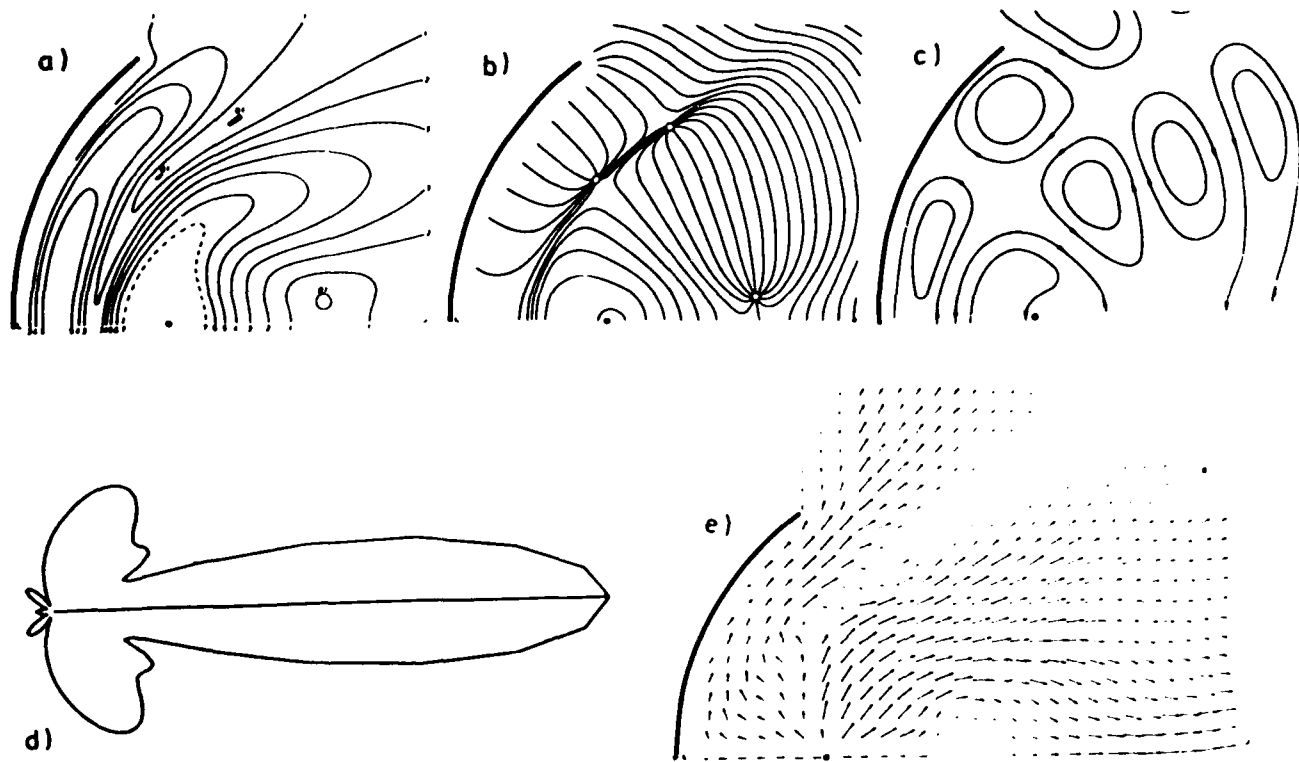
Figure 14   H-plane plots of a dipole-driven paraboloid-type spherical
reflector. (a) Lines of constant magnitude of the electric field,
(b) Phase fronts of the electric field, (c) Instantaneous
magnetic field lines, (d) Directional pattern, (e) Time averaged
Poynting's vector. After Monich[13].
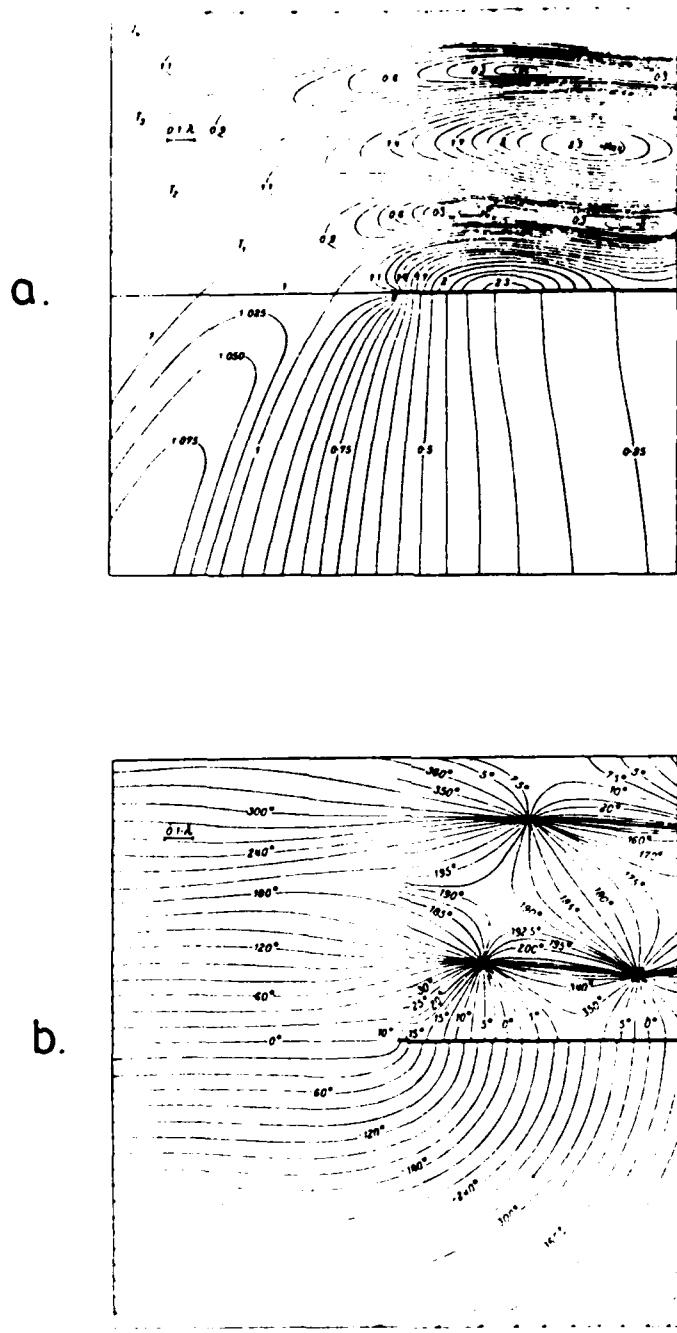
Figure 15   The diffraction of a normally incident H-polarised plane wave by
a perfectly conducting half-plane. (a) Amplitude contours, (b)
Phase contours. After Braunbek and Laukien[14].
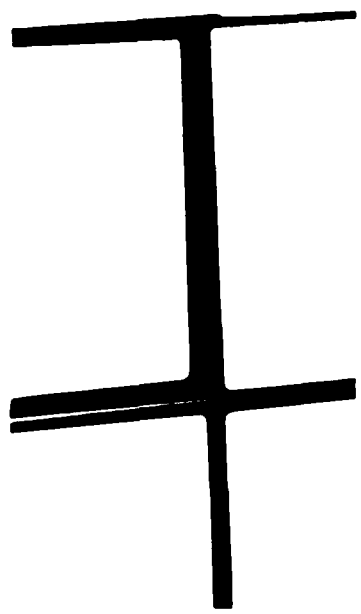
XYZ scanning rig, Microwave components and mirrors
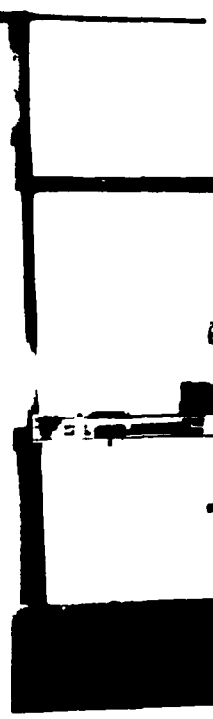
Scanning rig controller and data aquisition computer

Graphics and Analysis computer

Figure 16   General view of the 60 GHz microwave apparatus and computing equipment.

a   b   c   d   e   f.

|— 1cm
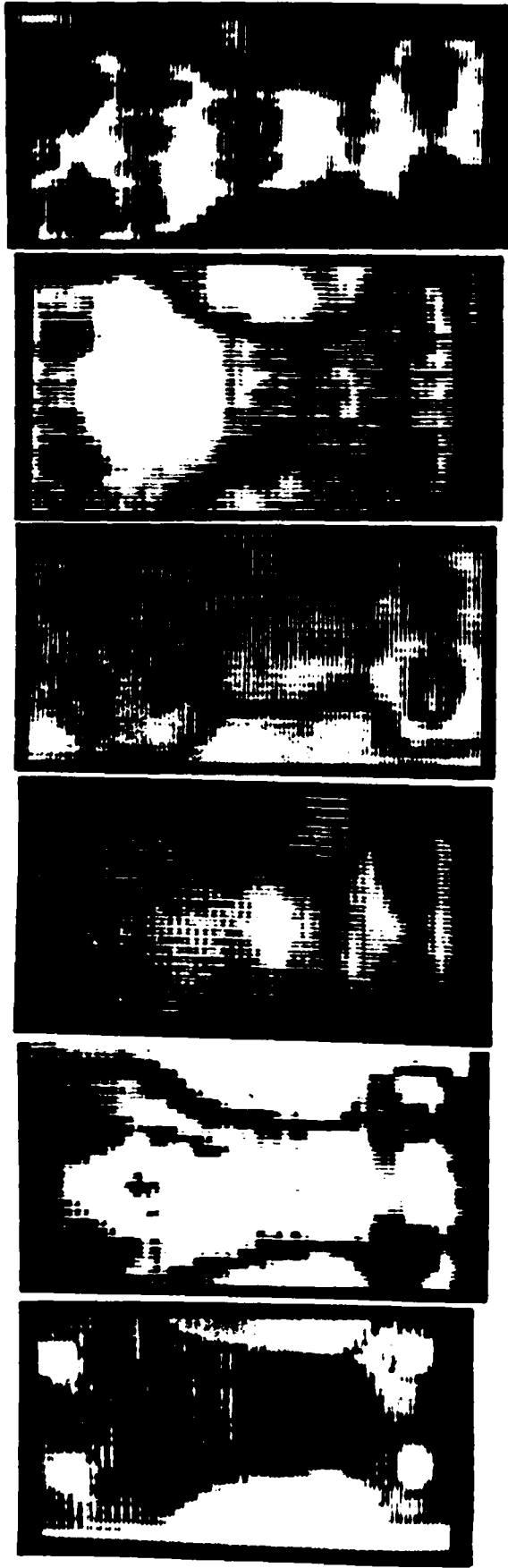
(a) Laser beam optical transmittance image of a laminate which has suffered delamination during reverse bend fatigue.
60GHz microwave transmittance images for the laminate from (a) using a rectangular aperture 2.5mmx6mm oriented with its long axis (b) parallel and (c) perpendicular to the long axis of the laminate, (d) using a circular aperture of diameter 3.5mm, (e) and (f) using a circular aperture of diameter 2.5mm with the long axis of the laminate oriented parallel and perpendicular to the incident microwave polarisation direction respectively.

a.
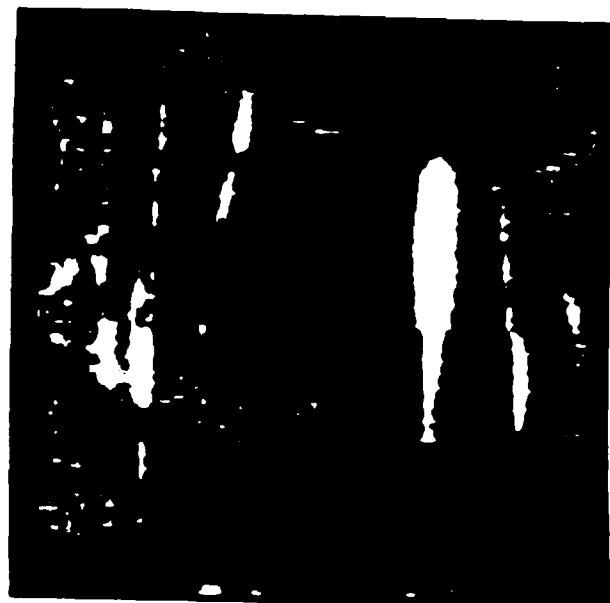
b.

c

d.

$\underbrace{\qquad\qquad}$
1 cm

Figure 18   Digitised subtracted images showing the changes in transmittance
for the 3 ply epoxy specimen after (a) 6×10^4,   (b) 1.6×10^5,
(c) 1.2×10^6 at 0.51% maximum strain,   and (d) after a further 6
$\times 10^4$ cycles at 1.1% maximum strain. The bright   regions   show
areas of   debonding and delamination.   (1 grey   level   increment
represents a 9% change in transmittance).
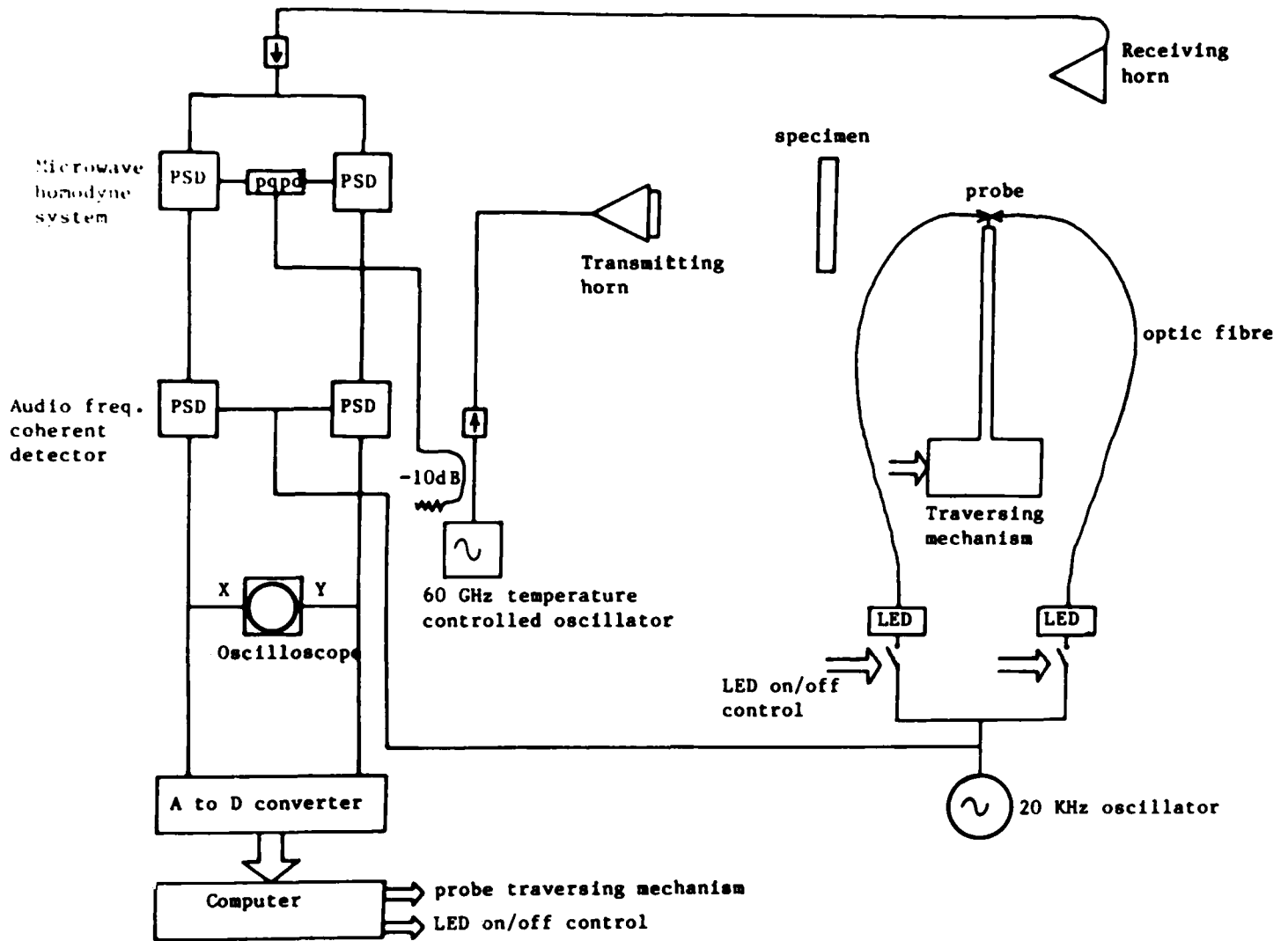
Figure 19 Schematic diagram showing the proposed electronic phase and polarisation sensitive detection system. After Hajnal[9].
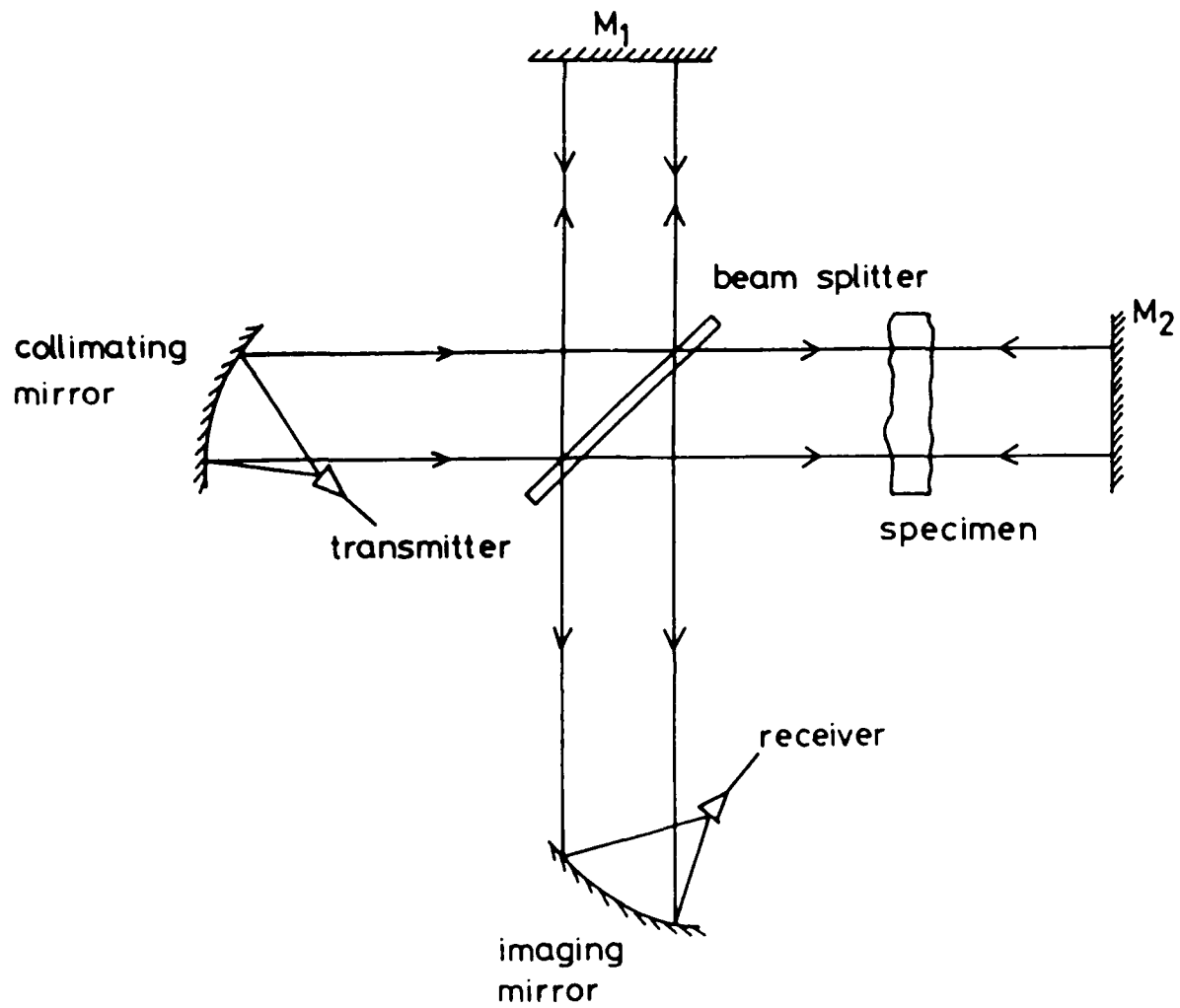
Figure 20   Twyman-Green interferometer arrangement for obtaining the phase
properties of the microwaves.
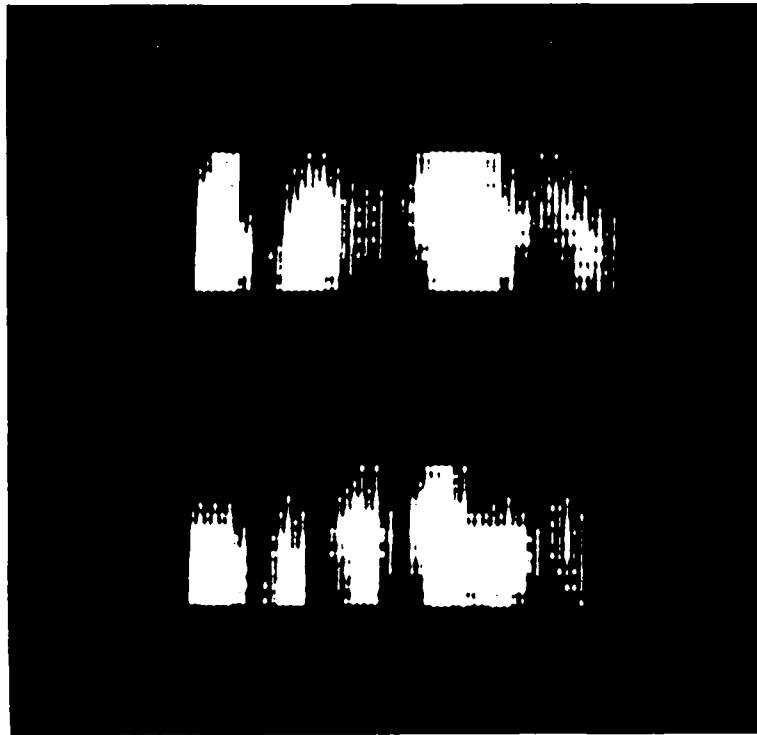
Figure 21   Microwave   interference   fringes   obtained   using   a   Fizeau
interferometer.
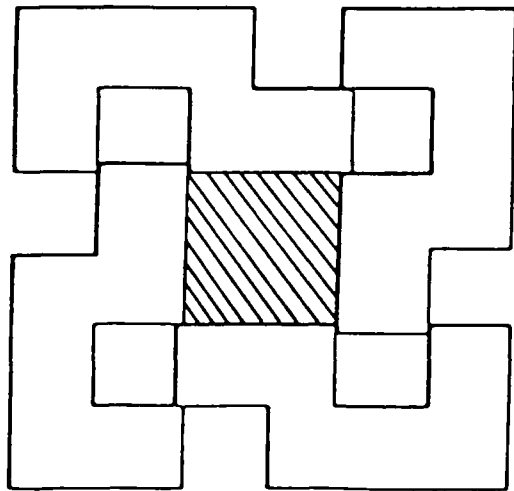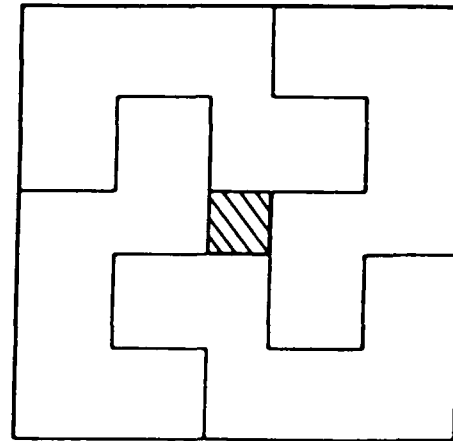
Open   Closed

Figure 22   One   arrangement   of gee-shaped anvils whereby rectangular   stock
             can   be   bi-dimensionally compressed. Anvils fully   opened   (a),
             fully closed (b)
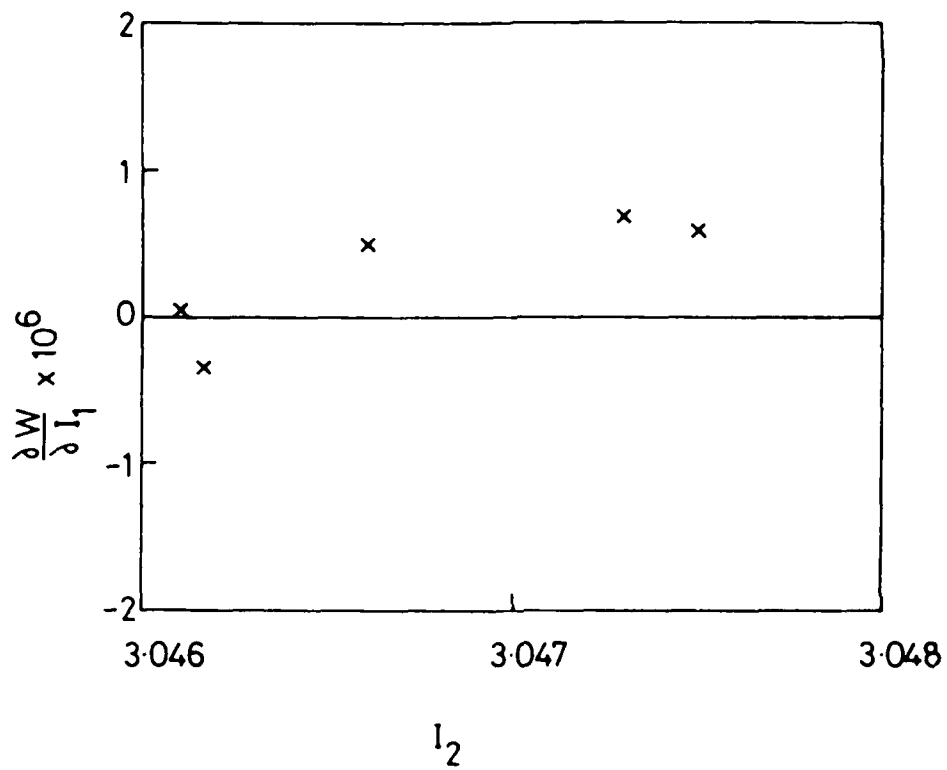
Figure 23   Plot of $\partial W/\partial I_1$ as a function of I_2 at constant I_1.
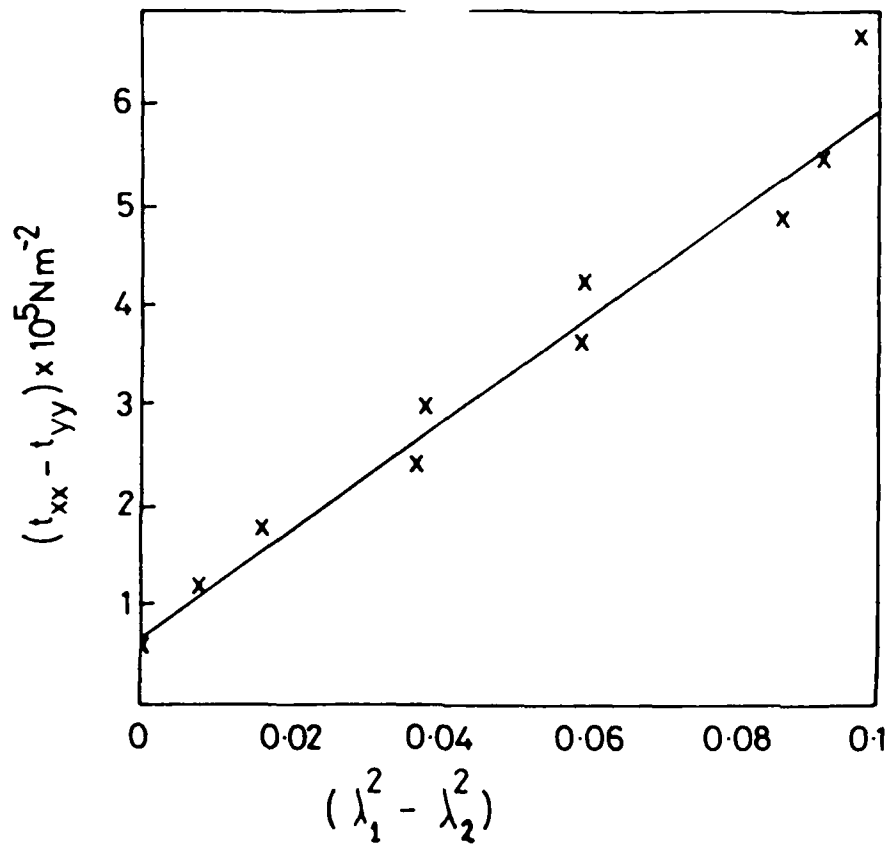
Figure 24   Plot of $t_{xx} - t_{yy}$ against $(\lambda_1^2 - \lambda_2^2)$

Figure 25   Bi-dimensional compression of chalk filled PVC. (a) undeformed
state, (b) and (c) after bi-dimensional compression.

a.

Figure 26   Stereo pair photomicrographs of sections taken from the specimens shown in Fig. 25(b). (a) parallel, and (b) perpendicular to the long axis of the deformed specimen.

Figure 26(b)